Mineralogical Magazine (2019), **83**, 655–671
doi:10.1180/mgm.2019.28

CAMBRIDGE UNIVERSITY PRESS

Article

Camanchacaite, chinchorroite, espadaite, magnesiofluckite, picaite and ríosecoite: six new hydrogen-arsenate minerals from the Torrecillas mine, Iquique Province, Chile

Anthony R. Kampf[1]*, Barbara P. Nash[2], Aaron J. Celestian[1], Maurizio Dini[3] and Arturo A. Molina Donoso[4]

[1]Mineral Sciences Department, Natural History Museum of Los Angeles County, 900 Exposition Boulevard, Los Angeles, CA 90007, USA; [2]Department of Geology and Geophysics, University of Utah, Salt Lake City, Utah 84112, USA; [3]Pasaje San Agustin 4045, La Serena, Chile; and [4]Los Algarrobos 2986, Iquique, Chile

Abstract

The new minerals camanchacaite, $NaCaMg_2[AsO_4]_2[AsO_3(OH)_2]$, chinchorroite, $Na_2Mg_5(As_2O_7)_2(AsO_3OH)_2(H_2O)_{10}$, espadaite, $Na_4Ca_3Mg_2[AsO_3(OH)]_2[AsO_2(OH)_2]_{10}(H_2O)_6{\cdot}H_2O$, magnesiofluckite, $CaMg(AsO_3OH)_2(H_2O)_2$, picaite, $NaCa[AsO_3OH][AsO_2(OH)_2]$ and ríosecoite, $Ca_2Mg(AsO_3OH)_3(H_2O)_2$, were discovered on two closely related specimens collected from the Torrecillas mine, Iquique Province, Chile. These minerals occur as secondary phases on massive quartz–hematite also in association with anhydrite, gypsum, halite and talmessite. Camanchacaite is monoclinic, $C2/c$, $a = 12.470(9)$, $b = 12.554(9)$, $c = 6.848(9)$ Å, $\beta = 113.75(2)°$, $V = 981.3(16)$ Å^3 and $Z = 4$. It has a protonated alluaudite-type structure. Chinchorroite is triclinic, $P\bar{1}$, $a = 8.7777(2)$, $b = 8.8570(3)$, $c = 9.7981(7)$ Å, $\alpha = 91.097(6)$, $\beta = 110.544(8)$, $\gamma = 103.167(7)°$, $V = 690.43(7)$ Å^3 and $Z = 1$. The structure contains abbreviated chains of five edge-sharing Mg octahedra that are linked by pyroarsenate and hydrogen-arsenate groups. Espadaite is orthorhombic, $Ccca$, $a = 12.3649(10)$, $b = 22.181(2)$, $c = 18.3292(13)$ Å, $V = 5027.1(7)$ Å^3 and $Z = 4$. The structure is based on heteropolyhedral sheets of formula $\{Ca_3Mg_2[AsO_3(OH)]_2[AsO_2(OH)_2]_{10}\}^{4-}$ that contain large voids; NaO_6 polyhedra occupy the interlayer region. Magnesiofluckite is triclinic, $P\bar{1}$, $a = 8.4143(6)$, $b = 7.5321(5)$, $c = 6.8917(4)$ Å, $\alpha = 82.477(6)$, $\beta = 97.682(6)$, $\gamma = 95.379(6)°$, $V = 427.84(5)$ Å^3 and $Z = 2$. It is isostructural with fluckite. Picaite is monoclinic, $P2_1/c$, $a = 7.2474(4)$, $b = 14.6547(7)$, $c = 7.2624(5)$ Å, $\beta = 99.520(7)°$, $V = 760.70(8)$ Å^3 and $Z = 4$. The structure contains chains of edge-sharing Na− and Ca octahedra with bridging $AsO_3(OH)$ and $AsO_2(OH)_2$ tetrahedra. Ríosecoite is triclinic, $P\bar{1}$, $a = 6.8110(9)$, $b = 7.3156(12)$, $c = 11.7773(17)$ Å, $\alpha = 83.466(6)$, $\beta = 84.394(6)$, $\gamma = 79.779(6)°$, $V = 571.95(15)$ Å^3 and $Z = 2$. The structure contains tetramers of edge-sharing CaO_7 and CaO_8 polyhedra linked by MgO_6 octahedra and bridging $AsO_3(OH)$ groups to form chains.

Keywords: camanchacaite, chinchorroite, espadaite, magnesiofluckite, picaite, ríosecoite, new mineral, hydrogen-arsenate, crystal structure, Torrecillas mine, Iquique Province, Chile

(Received 4 December 2018; accepted 11 April 2019; Accepted Manuscript online: 8 May 2019; Associate Editor: Irina O Galuskina)

Introduction

Though very limited in extent, the Torrecillas mine, a small, long-inactive mine in the northern Atacama Desert of Chile, has yielded a remarkable array of new secondary arsenic minerals. Five arsenites and twelve arsenates have now been approved as new minerals (Table 1). All of the new arsenates include hydrogen-arsenate and/or dihydrogen-arsenate groups. The last six of these arsenates, all of which occur on two closely related specimens, are described in this paper. The diversity of secondary arsenic phases also includes three already known arsenites and ten already known arsenates (Table 2).

The new mineral camanchacaite (\kɑ: mæn ˈkɑ: kɑ: aɪt\) is named for the 'camanchaca', a dense fog that forms along the northern Chilean coast where the Atacama Desert reaches the Pacific Ocean. The moisture particles that make up the fog are between 1 and 40 μm in diameter – too small to form raindrops. Consequently, the fog does not produce rain; however, the moisture it provides and its chemical content are likely to be responsible for at least some of the alteration of the As-bearing veins that yields secondary phases. Camanchacaite resembles the camanchaca fog in that it forms at Torrecillas (on the Atacama coast) as cloudy white balls, which contain OH but no H_2O.

The name chinchorroite is for the Chinchorro culture of the inhabitants of the coastal region of northern Chile and southern Peru from 9000 to 3500 years BP that includes the area around Torrecillas. The Chinchorro people are best known for their elaborate burial practices, which involved mummification. Analysis of hair samples from Chinchorro mummies has shown that the Chinchorro people suffered extensively from arsenic poisoning due to their consumption of water contaminated by arsenic. It has been suggested that the Chinchorro practice of mummification began as a response to miscarriages and premature deaths that were caused by arsenic poisoning (c.f. Arriaza *et al.*, 2010; Byrne *et al.*, 2010).

The name espadaite (/es ˈpa da aɪt/) is from the Spanish word *espada*, meaning sword, in allusion to the shape of the crystals.

*Author for correspondence: Anthony R. Kampf, Email: akampf@nhm.org
Cite this article: Kampf A.R., Nash B.P., Celestian A.J., Dini M. and Molina Donoso A.A. (2019) Camanchacaite, chinchorroite, espadaite, magnesiofluckite, picaite and ríosecoite: six new hydrogen-arsenate minerals from the Torrecillas mine, Iquique Province, Chile. *Mineralogical Magazine* **83**, 655–671. https://doi.org/10.1180/mgm.2019.28

Table 1. New secondary arsenic minerals from the Torrecillas mine.

Mineral	Ideal formula	IMA number	Reference
Arsenites			
Torrecillasite	$Na(As_2O_3)_2Cl$	2013-112	Kampf *et al.* (2014*a*)
Gajardoite	$K_2Ca(As_2O_3)_4Cl_4{\cdot}12H_2O$	2015-040	Kampf *et al.* (2016*a*)
Cuatrocapaite-(NH_4)	$(NH_4,K)_3(Na,Mg)_3(As_2O_3)_6Cl_6{\cdot}16H_2O$	2018-083	Kampf *et al.* (2018*a*)
Cuatrocapaite-(K)	$(K,NH_4)_3(Na,Mg)_3(As_2O_3)_6Cl_6{\cdot}16H_2O$	2018-084	Kampf *et al.* (2018*b*)
Mauriziodiniite	$NH_4(As_2O_3)_2I$	2019-036	Kampf *et al.* (2019)
Arsenates			
Magnesiokoritnigite	$Mg(AsO_3OH)(H_2O)$	2013-049	Kampf *et al.* (2013)
Canutite	$NaMn_3[AsO_4][AsO_3(OH)]_2$	2013-070	Kampf *et al.* (2014*b*)
Chongite	$Ca_3Mg_2(AsO_3OH)_2(AsO_4)_2(H_2O)_4$	2015-039	Kampf *et al.* (2016*b*)
Juansilvaite	$Na_5Al_3[AsO_3(OH)]_4[AsO_2(OH)_2]_2(SO_4)_2(H_2O)_4$	2015-080	Kampf *et al.* (2017*a*)
Currierite	$Na_4Ca_3Mg(Al,Fe)_4(AsO_3OH)_{12}(H_2O)_6{\cdot}3H_2O$	2016-030	Kampf *et al.* (2017*b*)
Magnesiocanutite	$NaMnMg_2[AsO_4][AsO_3(OH)]_2$	2016-057	Kampf *et al.* (2017*c*)
Camanchacaite	$NaCaMg_2[AsO_4][AsO_3(OH)]_2$	2018-025	This study
Chinchorroite	$Na_2Mg_5(As_2O_7)_2(AsO_3OH)_2(H_2O)_{10}$	2017-106	This study
Espadaite	$Na_4Ca_3Mg_2[AsO_3(OH)]_2[AsO_2(OH)_2]_{10}(H_2O)_6{\cdot}H_2O$	2018-089	This study
Magnesiofluckite	$CaMg(AsO_3OH)_2(H_2O)_2$	2017-103	This study
Picaite	$NaCa[AsO_3OH][AsO_2(OH)_2]$	2018-022	This study
Ríosecoite	$Ca_2Mg(AsO_3OH)_3(H_2O)_2$	2018-023	This study

Table 2. Other secondary arsenic minerals occurring at the Torrecillas mine.

Mineral	Ideal formula
Arsenites	
Arsenolite	As_2O_3
Claudetite	As_2O_3
Lucabindiite	$K(As_2O_3)_2Cl$
Arsenates	
Chudobaite	$Mg_5(AsO_4)_2(HAsO_4)_2{\cdot}10H_2O$
Hörnesite	$Mg_3(AsO_4)_2{\cdot}8H_2O$
Lavendulan	$NaCaCu_5(AsO_4)_4Cl{\cdot}5H_2O$
Mahnertite	$NaCu_3(AsO_4)_2Cl{\cdot}5H_2O$
Mansfieldite	$AlAsO_4{\cdot}2H_2O$
Natropharmacoalumite	$NaAl_4(AsO_4)_3(OH)_4{\cdot}4H_2O$
Natropharmacosiderite	$NaFe_4^{3+}(AsO_4)_3(OH)_4{\cdot}6\text{-}7H_2O$
Scorodite	$Fe^{3+}AsO_4{\cdot}2H_2O$
Talmessite	$Ca_2Mg(AsO_4)_2{\cdot}2H_2O$
Wendwilsonite	$Ca_2Mg(AsO_4)_2{\cdot}2H_2O$

The name magnesiofluckite signifies that the mineral is the Mg analogue of fluckite, $CaMn^{2+}(AsO_3OH)_2(H_2O)_2$ (Bari *et al.*, 1980; Catti *et al.*, 1980), with Mg in place of Mn^{2+}.

The name picaite (/ˈpi: kə aɪt/) is for the Pica (or Pica–Tarapacá) culture, which occupied the Atacama desert in northern Chile from ~900 CE until being subsumed by the Inca Empire ~1500 CE. Pica peoples were skilled at working with wood and marine-related objects, weaving and extracting rocks and minerals, used principally for decorative purposes. Pica settlements reached from the eastern Tamarugal Pampa on the east to the coast on the west and from the El Loa River on the south almost to Iquique on the north. Their coastal settlements included Salar Grande, Punta Lobos (~6 km SW of Torrecillas) and several of the small bays south of Iquique. Notably, Quebrada de Pica, a dry river canyon, reaches the Pacific Ocean immediately south of Torrecillas Hill.

The name ríosecoite (/ri: oʊ ˈseɪ koʊ aɪt/) is for Caleta Río Seco (Río Seco Cove), which is at the SW base of Torrecillas Hill, and for the small town of Río Seco, which is ~2.5 km SW of the Torrecillas mine. 'Río seco' means dry river in Spanish and, in this case, refers to the river that formed Quebrada de Pica, which reaches the Pacific Ocean at Caleta Rio Seco.

The new minerals and their names have been approved by the International Mineralogical Association. The type specimens upon which the descriptions are based are deposited in the collections of the Natural History Museum of Los Angeles County, 900 Exposition Boulevard, Los Angeles, CA 90007, USA. Specimen number 67257 is the holotype for chinchorroite, magnesiofluckite and ríosecoite, and a cotype for camanchacaite and picaite. Specimen 67285 is the holotype for espadaite and a cotype for picaite. Additional cotypes for camanchacaite are specimens 66771, 66772, 66773 and 66774.

Occurrence

The new minerals were all found on two closely related specimens collected at the Torrecillas mine, Salar Grande, Iquique Province, Tarapacá Region, Chile (~20°58'13"S, 70°8'17"W). Torrecillas Hill, on which the Torrecillas mine is located, is composed of four different rock units. The Coastal Range Batholith (mainly gabbros) extends from the seashore to the Pan-American Road along the base of Torrecillas Hill. At the foot of Torrecillas Hill is a small area of contact metamorphic rocks in which garnet crystals occur in metamorphosed shales. Higher on the hill, the rocks are predominantly porphyritic andesitic lavas of the Jurassic La Negra Formation (García, 1967; Buchelt and Tellez, 1988). The Torrecillas deposit, in which the new minerals were found, consists of two main veins rich in secondary arsenic and copper minerals that intersect metamorphosed marine shales and lavas. These mineralised veins are genetically related to the aforementioned porphyritic andesitic lavas of the Jurassic La Negra Formation. More information on the geology and mineralogy of the area is provided by Gutiérrez (1975).

The rare secondary chlorides, arsenates and arsenites were found at three main sites on the hill: an upper pit ~8 m long and 3 m deep, a lower pit ~100 m from the upper pit and ~5 m long and 3 m deep, and a mine shaft adjacent to the lower pit and lower on the hill. The two small specimens were found just inside the mine shaft by three of the authors (ARK, MD and AAMD) along with Jochen Schlüter and Joe Marty in February 2014.

The new minerals are low-temperature secondary phases occurring together on massive quartz–hematite also in association with anhydrite, gypsum, halite and talmessite. The secondary arsenic-rich assemblages at the Torrecillas deposit are interpreted as having formed under hyperarid conditions from the oxidation

Table 3. Physical and optical properties of camanchacaite, chinchorroite, espadaite, magnesiofluckite, picaite and ríosecoite.

	Camanchacaite	Chinchorroite	Espadaite	Magnesiofluckite	Picaite	Ríosecoite
Colour	colourless; pink–beige	colourless	colourless	colourless	colourless	colourless
Streak	white	white	white	white	white	white
Lustre	vitreous	vitreous	vitreous	vitreous	vitreous	vitreous
Transparency	transparent; translucent	transparent	transparent	transparent	transparent	transparent
Fluorescence	none	none	none	none	none	none
Mohs hardness	2½	2½	~2	2½	3½	3½
Fracture	splintery	curved, stepped	curved	irregular, stepped	curved, stepped	stepped
Tenacity	brittle	brittle	brittle	brittle	brittle	brittle
Cleavage	{010} & {101}, perfect*	{100} & {010}, very good	{001}, perfect	{010}, perfect; {100}, good	{010} & {001}, perfect	{010} & {001}, perfect
D_{meas} (g/cm^3)	n.d.	2.75(2)	2.73(2)	2.93(2)	3.00(2)	3.24(2)
D_{calc} (g/cm^3)	3.568	2.758	2.730	2.950	2.999	3.243
Chem. tests	soluble in dil. HCl	easily soluble in dil. HCl	easily soluble in dil. HCl	easily soluble in dil. HCl	easily soluble in dil. HCl	easily soluble in dil. HCl
Optical class	biaxial (+)	biaxial (+)	biaxial (–)	biaxial (+)	biaxial (–)	biaxial (–)
α	1.647(2)	1.546(2)	1.531(1)	1.588(2)	1.547(1)	1.637(1)
β	1.656(2)	1.560(2)	1.568(1)	1.599(2)	1.580(1)	1.651(1)
γ	1.685(2)	1.578(2)	1.574(1)	1.622(2)	1.604(1)	1.664(1)
$2V_{meas}$ (°)	60(10)	84(2)	44(1)	70(2)	80(1)	88(1)
$2V_{calc}$ (°)	59.1	83.7	43.0	70.2	79.4	87.2
Dispersion	$r < v$, slight	$r > v$, inclined, distinct	$r < v$, very slight	$r > v$, slight	$r > v$, slight	$r < v$, distinct
Orientation	$Z = \mathbf{b}$	$X \wedge \mathbf{a} = 4°$ $Y \wedge \mathbf{b} = 52°$ $Z \wedge \mathbf{c} = 20°$	$X = \mathbf{c}$ $Y = \mathbf{a}$ $Z = \mathbf{b}$	$X \wedge \mathbf{c} = 35°$ $Y \wedge \mathbf{a} = 16°$ $Z \wedge \mathbf{b} = 18°$	$Y = \mathbf{b}$ $X \wedge \mathbf{c} = 10°$ in obtuse β	$X \wedge \mathbf{b} \approx 18°$ $Y \wedge \mathbf{a} \approx 10°$ $Z \wedge \mathbf{c} \approx 48°$
Pleochroism	none	none	none	none	none	none
Gladstone–Dale compatibility	−0.029 = excellent	−0.012 = superior	−0.037 = excellent	−0.030 = excellent	−0.032 = excellent	−0.031 = excellent

* by analogy with other alluaudite-group minerals.

Fig. 1. Balls of camanchacaite on a yellow amorphous phase; note the broken ball of camanchacaite in the foreground. The field of view is 2.33 mm across, specimen #66772.

Fig. 2. Chinchorroite crystals with tiny currierite needles and balls of camanchacaite. The field of view is 0.7 mm across, specimen #67257.

of native arsenic, and possibly other As-bearing primary phases, coupled with reaction with fluids rich in dissolved Na, Ca and Mg. In earlier papers, we noted these fluids as resulting from evaporating meteoric water, as is the case for some other deposits in the Atacama region (*cf.* Cameron *et al.*, 2007); however, we now are convinced that the fluids are likely, at least in part, to be related to the frequent dense coastal fogs (*cf.* Rech *et al.*, 2003; Wang *et al.*, 2014). This mechanism of formation is discussed more fully below.

Appearance and properties

The physical and optical properties for all six minerals are listed in Table 3. The Mohs hardness was determined by scratch tests for all species except espadaite, which was estimated from the behaviour when broken. Densities were measured by flotation in mixtures of methylene iodide and toluene except for camanchacaite, which could not be measured because of inclusions. Optical studies for all minerals were done in white light and all, except camanchacaite, used a spindle stage for directly observing the optical indicatrix and measuring the indices of refraction. The crystal sizes, aggregations and morphologies are as follows:

Camanchacaite forms balls with compact radial structure to ~1 mm in diameter (Fig. 1). No crystal forms could be determined and no crystal fragments of adequate quality for single-crystal X-ray diffraction studies were found.

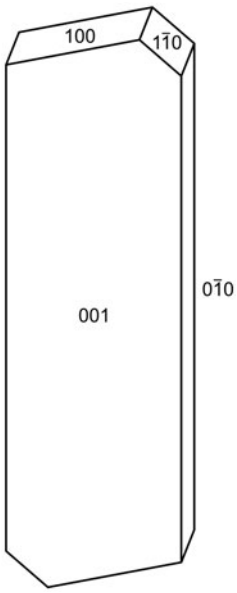

Fig. 3. Crystal drawing of chinchorroite; clinographic projection in nonstandard orientation, *a* vertical.

Fig. 4. Espadaite blades with balls of camanchacaite. The field of view is 0.84 mm across, specimen #67285.

Chinchorroite crystals are blades (Fig. 2) to ~1 mm in maximum dimension, which occur both isolated and in massive intergrowths. Tablets are flattened on {001}, elongate on [100] and exhibit the forms {100}, {010}, {001} and {1$\bar{1}$ 0} (Fig. 3). No twinning was observed.

Espadaite crystals are blades to ~0.2 mm long, forming fans, jumbled sprays and random intergrowths (Fig. 4). Blades are flattened on {001}, elongate on [100] and exhibit the forms {001}, {010}, {110} and {111} (Fig. 5). No twinning was observed.

Magnesiofluckite crystals are tablets and short blades to ~1 mm in maximum dimension, which are often grouped in tightly intergrown aggregates (Fig. 6). Tablets are flattened on {010}, slightly elongate on [001] and exhibit the forms {100}, {010}, {001}, {1$\bar{1}$0}, {101} and {10$\bar{1}$} (Fig. 7). No twinning was observed.

Picaite crystals are thick blades to ~1 mm long, typically in parallel intergrowths (Fig. 8). Blades are flattened on {100}, elongate on [001] and exhibit the forms {100}, {010}, {011}, {11$\bar{1}$} and {021} (Fig. 9). No twinning was observed.

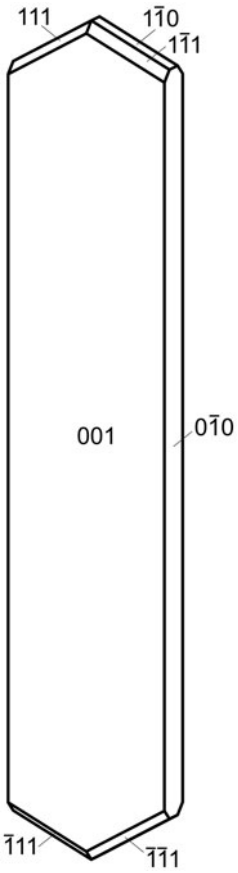

Fig. 5. Crystal drawing of espadaite; clinographic projection in nonstandard orientation, *a* vertical.

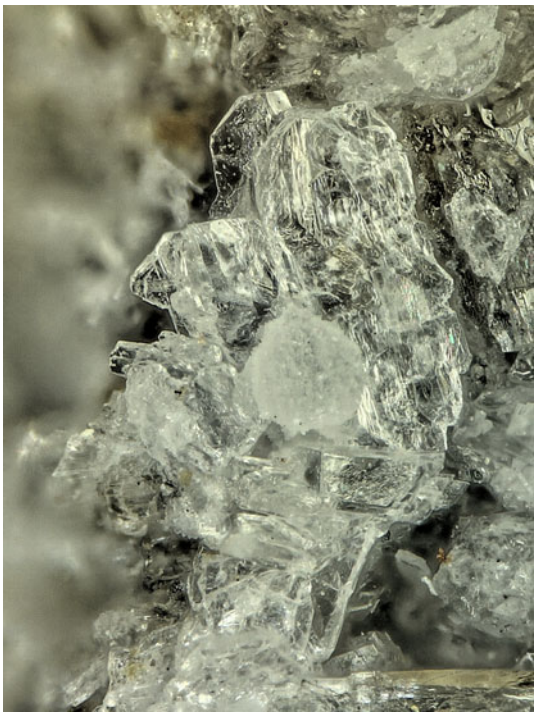

Fig. 6. Magnesiofluckite crystals with ball of camanchacaite. The field of view is 0.65 mm across, specimen #67257.

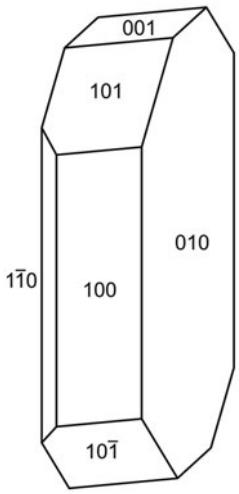

Fig. 7. Crystal drawing of magnesiofluckite; clinographic projection in standard orientation.

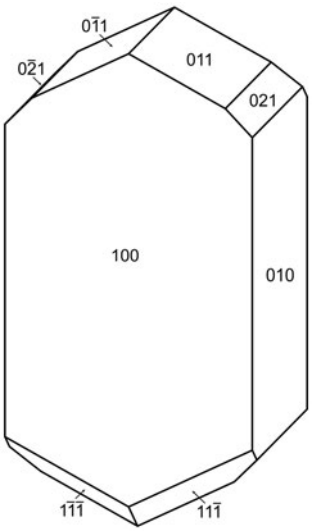

Fig. 9. Crystal drawing of picaite; clinographic projection in standard orientation.

Fig. 8. Picaite crystals with balls of camanchacaite. The field of view is 1.1 mm across, specimen #67285.

Fig. 10. Ríosecoite crystals with balls of camanchacaite. The field of view is 1 mm across, specimen #67257.

Ríosecoite crystals are prisms to ~1 mm long, elongated and striated on [100] with irregular terminations that commonly come to a somewhat rounded point. Only the prism forms {010} and {001} were observed. The prisms are often intergrown in subparallel bundles (Fig. 10). No twinning was observed.

Raman spectroscopy

Raman spectra from 4000 to 100 cm^{-1} were recorded using a Horiba XploRA PLUS with a 532 nm diode laser. The spectra for all phases were featureless between 2500 and 950 cm^{-1}. The background-removed spectra in the ranges 3700–2500 cm^{-1}, 965–715 cm^{-1} and 600–100 cm^{-1} are shown in stacked format in Fig. 11. The complete spectra in text format have been deposited with the Principal Editors of *Mineralogical Magazine* and are available as Supplementary material (see below). A listing of the positions of all fitted bands, including generalised mode assignments, is given in Table 4. Detailed mode characterisation, including comparisons with other arsenates, is beyond the scope of this paper; however, because we were unable to obtain a structure refinement for camanchacaite, it is worth mentioning that its Raman spectrum is quite similar to that of calciojohillerite, $NaCaMg_3(AsO_4)_3$ (Igor Pekov, *Pers. Comm.*; Pekov *et al.*, 2016), which is an unprotonated alluaudite-group mineral of similar composition.

Composition

Quantitative analyses were done at the University of Utah on a Cameca SX-50 electron microprobe with four wavelength-dispersive spectrometers using *Probe for EPMA* software. Analytical conditions were: 15 kV accelerating voltage, 10 nA beam current and a beam diameter of 10 μm. Counting times were 30 s on peak and 15 s on background for each element. In some cases, Na showed a time-dependent decrease in intensity under the electron beam, which was accounted for by an exponential fit to the intensity vs. time measurements and extrapolation to zero-time intensity. No other elements were detected by energy-dispersive spectroscopy. Other likely elements were sought by wavelength-dispersive spectroscopy scans, but none were above the detection limits. Raw X-ray intensities were corrected for matrix effects with a φ(ρz) algorithm (Pouchou and Pichoir, 1991). Because in all instances, insufficient material was available for a direct determination of H_2O, the amount of water was

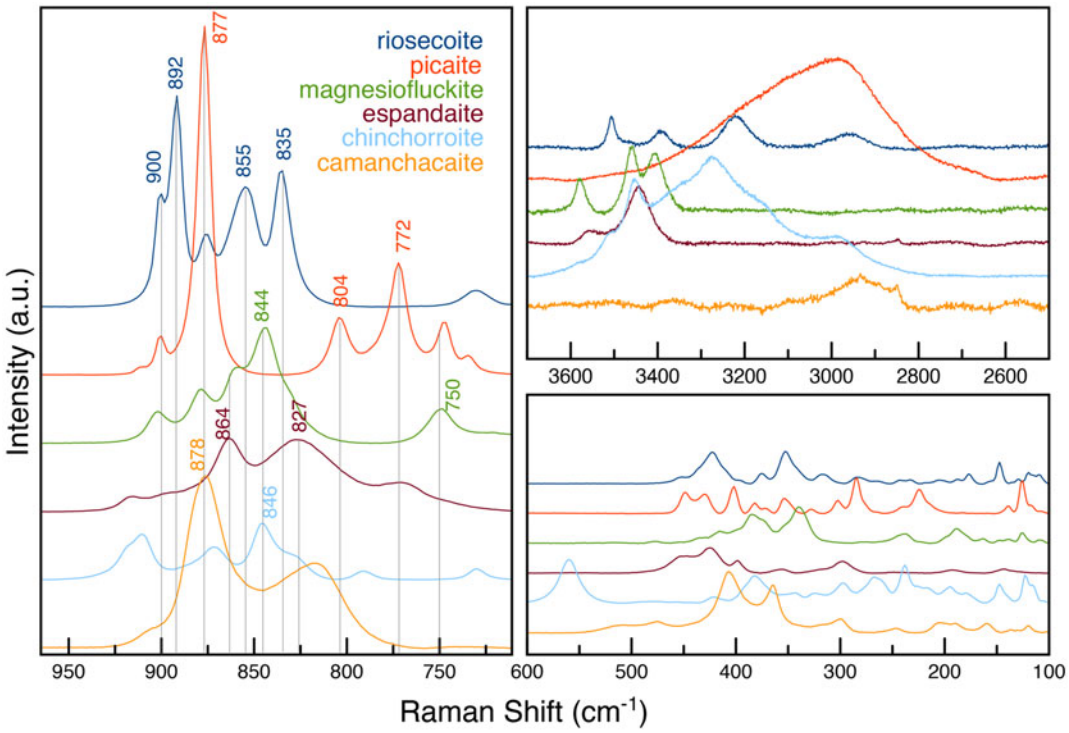

Fig. 11. Raman spectra of camanchacaite, chinchorroite, espadaite, magnesiofluckite, picaite and ríosecoite.

calculated on the basis of the crystal-structure analysis. Analytical data are given in Table 5 and empirical formulas are given in Table 6.

X-ray crystallography and structure refinement

Powder and single-crystal X-ray diffraction studies were done using a Rigaku R-Axis Rapid II curved-imaging-plate microdiffractometer, with monochromatic Mo*K*α radiation. For the powder diffraction (PXRD) studies, a Gandolfi-like motion on the φ and ω axes was used to randomise the polycrystalline samples and observed *d* values and intensities were derived by profile fitting using *JADE 2010* software (Materials Data, Inc.). For all species except camanchacaite, PXRD *d* values and intensities were calculated using *JADE 2010* based on the results of the single-crystal structure refinements (see below). For camanchacaite, calculated *d* values and intensities were obtained from a whole-pattern-fitting Rietveld refinement using *JADE 2010* based on the isotypic structure of magnesiocanutite as a starting point with the cations sites assigned as *A* = Na, *M*1 = Ca and *M*2 = Mg. Detailed listings of observed and calculated PXRD data for all six new species have been deposited with the Principal Editors of *Mineralogical Magazine* and are available as Supplementary material (see below).

Single-crystal structure studies were done for all species except camanchacaite. The Rigaku *CrystalClear* software package was used for processing the structure data, including the application of empirical multi-scan absorption corrections using *ABSCOR* (Higashi, 2001). Initial structure models for espadaite, picaite and riosecoite were obtained by the charge-flipping method using *SHELXT* (Sheldrick, 2015*a*), while those for chinchorroite and magnesiofluckite were obtained by direct methods using *SIR2011* (Burla *et al.*, 2012). *SHELXL-2016* (Sheldrick, 2015*b*) was used for the refinement of the structures. Full occupancies for the Na, Mg and Ca sites were assumed, except for the Na site in espadaite. The Na site refined to an occupancy of 0.891(12). Because the electron probe microanalysis results indicated a significant excess of Mg over what the Mg site can accommodate, the excess was assigned to the Na site and the Na occupancy was refined yielding a site occupancy of $(Na_{0.826(12)}Mg_{0.0625}\square_{0.111})$. Difference-Fourier maps revealed the location of all H atoms in the structures of chinchorroite, magnesiofluckite, picaite and ríosecoite, but not for the structure of espadaite because the small size of the crystal used gave a much smaller data set. Hydrogen atom positions were refined with soft restraints of 0.82(3) Å on the O–H distances and 1.30(3) Å on the H–H distances and with the U_{eq} of each H of the OH groups set to 1.5 times that of the donor O atom and the U_{eq} of each H of the H_2O groups set to 1.2 times that of the donor O atom. Cell parameters are reported in Table 7. Data collection and refinement details are given in Table 8. Atom coordinates and displacement parameters have been deposited with the Principal Editors of *Mineralogical Magazine* and are available as Supplementary material (see below). Selected bond distances are reported in Table 9 and bond-valence analyses in Table 10.

Descriptions of the structures

Camanchacaite

Camanchacaite is a member of the alluaudite group and is isostructural with compounds with the protonated alluaudite-type structure, including the minerals o'danielite, $NaZn_3[AsO_4][AsO_3(OH)]_2$ (Keller and Hess, 1988), groatite, $NaCaMn_2[PO_4][PO_3(OH)]_2$ (Cooper *et al.*, 2009), canutite, $NaMn_3[AsO_4][AsO_3(OH)]_2$ (Kampf *et al.*, 2014*b*), and

Table 4. Raman shifts (cm^{-1}) for camanchacaite, chinchorroite, espadaite, magnesiofluckite, picaite and ríosecoite.

Camanchacaite	Chinchorroite	Espadaite	Magnesiofluckite	Picaite	Riosecoite	Raman modes[1,2,3]
			109	107		Unspecified[4] lattice modes
	115			117		and *M*–O–As bending
120	123		125	126		
134		135	139	139	147	
	147	145	148		156	
160	179		163		177	
193	195	192	188		187	
					204	
				214		
	223		223	224		
	239		236		233	
248			245	242	243	
			252			
	266			270	266	
			278	276		
	298	298		285	283	
				302		
323	323	320		328	317	
			338		340	Unspecified[4] O–As–O symmetric
	343		345	349		and asymmetric bending of the
	353	357		355	353	$AsO_3(OH)$ and $AsO_2(OH)_2$ groups
367			373	372	375	
	382		384	382	397	
405		398	400	402	409	
			415			
	420	424	430	429	423	
440				442	435	
		451		450	450	
474		480	478			
511						
	559					As–O–As symmetric bridge stretching
	560					of the As_2O_7 group[3]
	563					
					704	Unspecified[4] As–O symmetric
	730		729	734	730	and asymmetric stretching
			750	747		of the As_2O_7, $AsO_3(OH)$
		760				and $AsO_2(OH)_2$ groups
		770		772		
789	791	788		775		
815				804		
836	830	827				
			844		835	As–O–As symmetric stretching
857	**846**		846		855	of the $AsO_3(OH)$ & As_2O_7 groups[3]
		864	862			
878	871		879	**877**	876	
		881		878		
					892	
903		896	901	900	900	
		916		911		
	910					As–O–As asymmetric bridge
	912					stretching for the As_2O_7 groups[3]
	918					
2851						Unspecified[4] O–H symmetric
2929	2978				2965	and asymmetric stretching
3060	3033			3007		
	3177			3180		
	3268			3274	3219	
	3328		3406	3404	3392	
	3455	3443	3462		3484	
	3510					
	3579	3543	3578		3507	

[1] Bold numbers indicate the most intense band in each spectrum.
[2] Compared to austinite, adamite, paradamite, kottigite, mimetite, wendelwilsonite from Caracas and Bobocioiu (2011).
[3] Compared to synthetic $Sr_5(As_2O_7)_2(AsO_3OH)$ from Mihajlović *et al.* (2004).
[4] Due to the complexity of the crystal structures, we are unable to assign all bands to specific Raman mode vibrational types.

Table 5. Chemical analyses [mean (std. dev.) range in wt.%] for camanchacaite, chinchorroite, espadaite, magnesiofluckite, picaite and ríosecoite.

	Camanchacaite	Chinchorroite	Espadaite	Espadaite (norm.)*	Magnesiofluckite	Picaite	Ríosecoite
	14 points on 5 crystals	7 points on 3 crystals	4 points on 4 crystals		9 points on 3 crystals	14 points on 3 crystals	12 points on 5 crystals
Na_2O	5.78 (0.31)	5.03 (0.33)	4.39 (0.23)	4.95	0.12 (0.07)	8.99 (0.23)	0.07 (0.02)
	5.14–6.46	4.58–5.66	4.11–4.59		0.03–0.24	8.69–9.37	0.02–0.11
CaO	8.87 (0.58)	0.06 (0.04)	7.89 (0.17)	8.15	14.53 (0.40)	16.05 (0.60)	19.74 (0.32)
	7.87–9.62	0.01–0.12	7.78–8.14		13.94–15.19	15.48–17.05	19.40–20.40
MgO	16.06 (0.62)	17.39 (0.35)	4.24 (0.05)	4.38	10.59 (0.42)	0.18 (0.05)	6.95 (0.29)
	15.19–17.07	17.10–18.15	4.18–4.30		9.86–11.40	0.11–0.29	6.43–7.31
MnO	0.24 (0.22)	–	–	–	–	–	–
	0.02–0.75						
As_2O_5	65.22 (0.61)	60.33 (0.90)	64.60 (0.19)	66.74	60.32 (0.85)	66.87 (0.84)	61.59 (0.23)
	64.48–66.26	59.10–62.00	64.34–64.77		58.85–61.29	65.32–68.25	61.26–61.91
H_2O§	3.57	17.54		15.78	14.20	7.88	11.45
Total	99.74	100.35		100.00	99.76	99.97	99.80

* The poor quality of the espadaite crystal surfaces and significant beam damage provided low analyses for all components especially Na; consequently, Na_2O was calculated from the structure and the other components were normalised to a total of 100%.

§ H_2O was calculated for all analyses based upon the structures.

Table 6. Empirical formulas of camanchacaite, chinchorroite, espadaite, magnesiofluckite, picaite and ríosecoite.

Mineral	Empirical formula	Formula basis
Camanchacaite	$(Na_{0.99}Ca_{0.84}Mg_{2.11}Mn_{0.02})_{\Sigma 3.96}[AsO_4][AsO_{2.95}(OH)_{1.05}]_2$	3 As, charge balance and 12 O apfu
Chinchorroite	$(Na_{1.86}Ca_{0.01})_{\Sigma 1.87}Mg_{4.93}[As_2O_7]_2[AsO_{2.87}(OH)_{1.13}]_2(H_2O)_{10}$	2 As, charge balance and 10 O apfu
Espadaite	$(Na_{0.83}Mg_{0.06}\square_{0.11})_4Ca_{3.00}Mg_{2.00}[AsO_3OH]_{1.80}[AsO_2(OH)_2]_{10.20}(H_2O)_6{\cdot}H_2O$	12 As, charge balance and 55 O apfu
Magnesiofluckite	$(Ca_{0.99}Na_{0.01})_{\Sigma 1.00}Mg_{1.00}[AsO_3OH]_2(H_2O)_2$	2 As, charge balance and 10 O apfu
Picaite	$(Na_{1.00}Ca_{0.98}Mg_{0.02})_{\Sigma 2.00}[AsO_3OH][AsO_2(OH)_2]$	2 As, charge balance and 8 O apfu
Ríosecoite	$(Ca_{1.97}Mg_{0.97}Na_{0.01})_{\Sigma 2.95}[AsO_{2.96}(OH)_{1.04}]_3(H_2O)_2$	3 As, charge balance and 14 O apfu

Table 7. Crystallographic properties of camanchacaite, chinchorroite, espadaite, magnesiofluckite, picaite and ríosecoite.

	Camanchacaite	Chinchorroite	Espadaite	Magnesiofluckite	Picaite	Ríosecoite
Space group	*C*2/*c*	$P\bar{1}$	*Ccca*	$P\bar{1}$	$P2_1/c$	$P\bar{1}$
a (Å)	12.470(9)	8.7777(2)	12.3649(10)	8.4143(6)	7.2474(4)	6.8110(9)
b (Å)	12.554(9)	8.8570(3)	22.181(2)	7.5321(5)	14.6547(7)	7.3156(12)
c (Å)	6.848(9)	9.7981(7)	18.3292(13)	6.8917(4)	7.2624(5)	11.7773(17)
α (°)	90°	91.097(6)	90°	82.477(6)	90°	83.466(6)
β (°)	113.75(2)°	110.544(8)	90°	97.682(6)	99.520(7)	84.394(6)
γ (°)	90°	103.167(7)	90°	95.379(6)	90°	79.779(6)
V (Å^3)	981.3(16)	690.43(7)	5027.1(7)	427.84(5)	760.70(8)	571.95(15)
Z	4	1	4	2	4	2

Table 8. Details of structure refinements for chinchorroite, espadaite, magnesiofluckite, picaite and ríosecoite.

	Chinchorroite	Espadaite	Magnesiofluckite	Picaite	Ríosecoite
Absorption coefficient (mm^{-1})	7.449	8.361	8.519	9.522	9.744
F(000)	558	3988.5	368	656	540
Crystal size (μm)	200 × 100 × 20	100 × 60 × 20	180 × 180 × 80	150 × 90 × 40	130 × 60 × 30
θ range	3.03 to 27.44°	3.30 to 23.26°	3.00 to 27.47°	3.17 to 27.48°	3.19 to 27.47°
Index ranges	$-11 \le h \le 11$	$-12 \le h \le 13$	$-10 \le h \le 10$	$-8 \le h \le 9$	$-7 \le h \le 8$
	$-11 \le k \le 11$	$-24 \le k \le 24$	$-9 \le k \le 9$	$-18 \le k \le 19$	$-9 \le k \le 9$
	$-12 \le l \le 12$	$-20 \le l \le 18$	$-8 \le l \le 8$	$-9 \le l \le 8$	$-15 \le l \le 15$
Reflections collected / unique	15,442 / 3144	8437 / 1802	7507 / 1942	7758 / 1732	10,316 / 2611
R_{int}	0.047	0.099	0.040	0.035	0.059
Reflections [$I_o > 2\sigma I$]	2812	1304	1764	1557	2342
Completeness to θ_{max} (%)	99.7	99.3	99.0	98.7	99.7
Parameters / restraints	238 / 15	188 / 0	145 / 8	118 / 3	202 / 9
GoF	1.063	1.041	1.085	1.173	1.058
Final *R* indices, [$I_o > 2\sigma I$]	$R_1 = 0.0266$	$R_1 = 0.0461$	$R_1 = 0.0253$	$R_1 = 0.0239$	$R_1 = 0.0261$
	$wR_2 = 0.0614$	$wR_2 = 0.1076$	$wR_2 = 0.0615$	$wR_2 = 0.0567$	$wR_2 = 0.0566$
R indices (all data)	$R_1 = 0.0313$	$R_1 = 0.0685$	$R_1 = 0.0282$	$R_1 = 0.0278$	$R_1 = 0.0307$
	$wR_2 = 0.0636$	$wR_2 = 0.1186$	$wR_2 = 0.0631$	$wR_2 = 0.0591$	$wR_2 = 0.0587$
Peak / hole (e^-/Å^3)	+0.84 / −0.62	+0.85 / −0.79	+0.76 / −0.61	+1.32 / −0.66	+0.78 / −0.61

magnesiocanutite, $NaMnMg_2[AsO_4]_2[AsO_2(OH)_2]$ (Kampf *et al.*, 2017*c*). The general formula of these phases is $AM1M2_2[T1O_4][T2O_3(OH)]_2$ {*T* = P or As}, where the *M*1 and *M*2 octahedra link by edge-sharing to form staggered chains, *T*1 and *T*2 tetrahedra cross-link the chains, and *A* cations occupy large channel sites. In camanchacaite, *A* = Na, *M*1 = Ca and *M*2 = Mg. The crystal structure of canutite is shown in Fig. 12.

Chinchorroite

The structure of chinchorroite contains two types of arsenate groups. The As1 and As2 tetrahedra share a common vertex (O4) forming an As_2O_7 pyroarsenate (diarsenate) group. The As3 tetrahedron is an AsO_3OH acid (protonated) arsenate group. Another unusual feature of the chinchorroite structure is an abbreviated chain of five edge-sharing MgO_6 octahedra that includes one Mg1, two Mg2 and two Mg3 octahedra, all of which exhibit regular geometry. Both the As_2O_7 and AsO_3OH groups share corners with octahedra in this five-member chain segment (Fig. 13). An edge-sharing dimer of distorted Na octahedra shares edges with Mg2 and Mg3 octahedra in adjacent chain segments, linking them into a complex thick slab of edge-sharing Mg and Na octahedra parallel to $\{10\bar{1}\}$ (Fig. 14). The As_2O_7 and AsO_3OH groups further link the octahedra within these sheets and a single vertex (O7) of the As2 tetrahedron links to a Mg2/Mg3 octahedron vertex in an adjacent sheet, thereby creating a heteropolyhedral framework (Fig. 15).

Pyroarsenate groups have been reported previously in the structures of only two minerals: petewilliamsite, $(Ni,Co)_{30}(As_2O_7)_{15}$ (Roberts *et al.*, 2004) and theoparacelsite, $Cu_3(OH)_2As_2O_7$ (Sarp and Černy, 2001). However, no other mineral structure has been

Table 9. Selected bond distances (Å) and angles (°) for chinchorroite, espadaite, magnesiofluckite, picaite and ríosecoite.

Chinchoroite						Hydrogen bonds					
						D–H	*d*(*D*–H)	*d*(H···*A*)	*d*(*D*···*A*)	<*DHA*	*A*
Na–OW4	2.309(3)	Mg2–O1	2.025(2)	As1–O1	1.655(2)	OH–H	0.79(3)	1.90(3)	2.682(3)	170(4)	O3
Na–O1	2.353(3)	Mg2–O2	2.085(2)	As1–O2	1.668(2)	OW1–H1A	0.82(2)	1.88(2)	2.679(3)	163(4)	O3
Na–OW3	2.404(3)	Mg2–O10	2.094(2)	As1–O3	1.670(2)	OW1–H1B	0.81(2)	1.96(3)	2.725(3)	159(4)	O5
Na–OW2	2.465(3)	Mg2–OW1	2.112(3)	As1–O4	1.759(2)	OW2–H2A	0.83(2)	2.02(2)	2.839(4)	170(4)	OW3
Na–OW4	2.511(3)	Mg2–O7	2.140(2)	<As1–O>	1.688	OW2–H2B	0.80(2)	2.02(3)	2.801(3)	167(4)	O3
Na–O10	2.852(3)	Mg2–O6	2.149(2)			OW3–H3A	0.84(2)	2.04(3)	2.834(3)	159(4)	OW1
<Na–O>	2.482	<Mg2–O>	2.101	As2–O5	1.664(2)	OW3–H3B	0.82(2)	2.03(3)	2.840(3)	167(4)	O9
				As2–O6	1.669(2)	OW4–H4A	0.84(2)	2.00(3)	2.822(4)	166(4)	O8
Mg1–O2 ×2	2.061(2)	Mg3–O8	2.016(2)	As2–O7	1.674(2)	OW4–H4B	0.83(2)	2.24(4)	2.845(3)	129(4)	O5
Mg1–O9 ×2	2.073(2)	Mg3–OW5	2.080(3)	As2–O4	1.748(2)	OW5–H5A	0.81(3)	2.24(3)	2.960(4)	148(4)	OH
Mg1–O6 ×2	2.086(2)	Mg3–O5	2.098(2)	<As2–O>	1.689	OW5–H5B	0.80(3)	2.03(3)	2.812(3)	165(4)	O9
<Mg1–O>	2.073	Mg3–O7	2.130(2)								
		Mg3–O10	2.131(2)	As3–O8	1.657(2)						
		Mg3–OW2	2.166(3)	As3–O9	1.671(2)						
		<Mg3–O>	2.104	As3–O10	1.685(2)						
				As3–OH	1.735(2)						
				<As3–O>	1.687						

Espadaite						Hydrogen bonds	
Na–OW2 ×½	2.34(3)	Ca1–O6 ×4	2.455(6)	As1–O1	1.667(6)	OH3···OH3	2.472(11)
Na–OW1	2.371(7)	Ca1–O10 ×4	2.589(5)	As1–O2	1.669(5)	OH4···O9	2.536(8)
Na–OH12	2.478(8)	<Ca1–O>	2.522	As1–OH3	1.699(6)	OH7···O1	2.475(8)
Na–OH7	2.491(8)			As1–OH4	1.722(5)	OH8···OH3	2.686(8)
Na–OH4	2.499(7)	Ca2–O1 ×2	2.378(6)	<As1–O>	1.689	OH11···O6	2.533(9)
Na–OW2 ×½	2.53(4)	Ca2–O9 ×2	2.392(5)			OH12···OW3	2.945(7)
Na–OH8	2.730(8)	Ca2–O2 ×2	2.532(5)	As2–O5	1.663(5)	OW1···O6 ×2	2.928(10)
<Na–O>	2.500	Ca2–O5 ×2	2.627(5)	As2–O6	1.668(6)	OW2···OH11	2.828(19)
		<Ca2–O>	2.482	As2–OH7	1.696(6)	OW2···OW4b	2.99(5)
Mg–O5 ×2	2.034(5)			As2–OH8	1.729(6)	OW3···OH3 ×2	2.777(7)
Mg–O2 ×2	2.085(6)			<As2–O>	1.689		
Mg–O10 ×2	2.100(6)						
<Mg–O>	2.073			As3–O9	1.645(5)		
				As3–O10	1.665(5)		
				As3–OH11	1.705(6)		
				As3–OH12	1.729(7)		
				<As3–O>	1.686		

Magnesiofluckite						Hydrogen bonds					
						D–H	*d*(*D*–H)	*d*(H···*A*)	*d*(*D*···*A*)	<*DHA*	*A*
Ca–O2	2.312(2)	Mg–OW10	2.045(3)	As1–O2	1.661(2)	OH1–H1	0.80(3)	2.22(3)	2.976(3)	158(5)	O3
Ca–O5	2.329(2)	Mg–O7	2.098(2)	As1–O4	1.672(2)	OH8–H8	0.80(3)	1.83(3)	2.611(3)	168(4)	O4
Ca–O2	2.330(2)	Mg–O4	2.101(2)	As1–O3	1.680(2)	OW9–H9A	0.81(2)	2.05(3)	2.860(3)	174(4)	OH8
Ca–OW9	2.362(3)	Mg–O3	2.114(2)	As1–OH1	1.743(2)	OW9–H9B	0.83(3)	2.39(3)	3.038(3)	136(4)	OW10
Ca–O3	2.378(2)	Mg–O6	2.126(2)	<As–O>	1.689	OW10–H10A	0.82(2)	2.11(3)	2.861(3)	151(4)	OH8
Ca–O6	2.415(2)	Mg–O7	2.185(2)			OW10–H10B	0.84(2)	1.82(3)	2.633(3)	165(4)	O5
<Ca–O>	2.354	<Mg–O>	2.112	As2–O5	1.660(2)						
				As2–O6	1.676(2)						
				As2–O7	1.680(2)						
				As2–OH8	1.731(2)						
				<As–O>	1.687						

Picaite						Hydrogen bonds					
						D–H	*d*(*D*–H)	*d*(H···*A*)	*d*(*D*···*A*)	<*DHA*	*A*
Ca–O6	2.305(2)	Na–O5	2.307(3)	As1–O1	1.644(2)	OH3–H3	0.84(3)	1.74(3)	2.565(3)	169(4)	O6
Ca–O5	2.315(2)	Na–OH8	2.349(3)	As1–O2	1.660(2)	OH4–H4	0.87(3)	1.76(3)	2.620(3)	171(4)	O7
Ca–O1	2.346(2)	Na–O1	2.352(2)	As1–OH3	1.712(2)	OH8–H8	0.83(2)	1.91(3)	2.722(3)	165(4)	O7
Ca–O7	2.376(2)	Na–OH4	2.458(2)	As1–OH4	1.730(2)						
Ca–O2	2.379(2)	Na–OH3	2.479(3)	<As1–O>	1.687						
Ca–O2	2.394(2)	Na–OH4	2.882(3)								
<Ca–O>	2.353	<Na–O>	2.471	As2–O5	1.652(2)						
				As2–O6	1.660(2)						
				As2–O7	1.686(2)						
				As2–OH8	1.732(2)						
				<As1–O>	1.683						

Ríosecoite						Hydrogen bonds					
						D–H	*d*(*D*–H)	*d*(H···*A*)	*d*(*D*···*A*)	<*DHA*	*A*
Mg–OW13	2.027(3)	Ca1–O2	2.334(3)	Ca2–O1	2.336(3)	OH4–H4	0.80(3)	1.89(3)	2.683(4)	172(4)	O9
Mg–O7	2.076(3)	Ca1–O10	2.375(2)	Ca2–O2	2.420(3)	OH8–H8	0.79(3)	2.13(4)	2.764(4)	137(5)	OH12
Mg–O3	2.097(3)	Ca1–O5	2.449(3)	Ca2–O9	2.432(3)	OH12–H12	0.78(3)	1.98(3)	2.743(4)	163(5)	O7
Mg–O10	2.122(3)	Ca1–O11	2.458(2)	Ca2–O11	2.449(3)	OW13–H13A	0.81(2)	1.91(3)	2.715(4)	168(4)	OW14
Mg–O5	2.138(3)	Ca1–O1	2.461(2)	Ca2–O6	2.473(3)	OW13–H13B	0.80(2)	2.02(3)	2.733(4)	148(4)	OH8
Mg–O6	2.162(3)	Ca1–OW1	2.467(3)	Ca2–O11	2.539(3)	OW14–H14A	0.81(2)	2.15(3)	2.904(4)	156(4)	O7
<Mg–O>	2.104	Ca1–OH4	2.495(3)	Ca2–O3	2.614(3)	OW14–H14B	0.82(2)	1.84(2)	2.646(4)	169(4)	O3
		Ca1–OH12	2.895(3)	<Ca2–O>	2.646						
		<Ca1–O>	2.492								
As1–O1	1.656(2)	As2–O5	1.668(2)	As3–O9	1.660(2)						
As1–O2	1.661(2)	As2–O6	1.672(2)	As3–O10	1.667(2)						
As1–O3	1.678(2)	As2–O7	1.676(2)	As3–O11	1.681(2)						
As1–OH4	1.742(2)	As2–OH8	1.737(3)	As3–OH12	1.749(3)						
<As1–O>	1.684	<As2–O>	1.688	<As3–O>	1.689						

reported to contain both pyroarsenate and hydrogen-arsenate groups and we are aware of only one synthetic phase $Sr_5(As_2O_7)_2(AsO_3OH)$ containing both of these structural units (Mihajlović *et al.*, 2004). The chain of five edge-sharing Mg octahedra is similar to the five-member chain segment of edge-sharing Al octahedra in the structure of matulaite, $Fe^{3+}Al_7(PO_4)_4(PO_3OH)_2(OH)_8(H_2O)_8{\cdot}8H_2O$, (Kampf *et al.*, 2012), although in matulaite, each end of the chain segment has an additional corner-linked Al octahedron and the PO_4 and PO_3OH tetrahedra decorating the chain are configured differently (Fig. 13).

Espadaite

The structure of espadaite contains one NaO_6 polyhedron (highly distorted octahedron with a split OW2 vertex), one MgO_6 octahedron, two different CaO_8 polyhedra and three different hydrogen arsenate groups. Although H atom sites could not be located in the structure refinement, it was possible to derive a complete hydrogen-bonding scheme (see Table 9), and resultant bond-valence sums (BVS) allowed assignment of O, OH and H_2O to each of the O sites (see Table 10). The OH3 site, in particular, presents an unusual situation. The OH3 site receives normal hydrogen bonds from OH8 (0.23 valence units) and OH12 (0.19 vu), and its close approach (2.472 Å) to an adjacent OH3 site is indicative of a symmetrical hydrogen bond between them, presumably sharing an H atom sited at the special position (½,½,0). The result is that OH3 has ½ O and ½ OH character. Assigning the As2 and As3 arsenate groups as dihydrogen arsenates and the As1 group as a half dihydrogen and half monohydrogen arsenate, results in an ideal formula with $[AsO_{2.5}(OH)_{1.5}]_4[AsO_2(OH)_2]_8^{14-}$, or alternatively $[AsO_3(OH)]_2[AsO_2(OH)_2]_{10}^{14-}$, as the anionic component, thereby balancing the charge of the ideal cation content of $[Na_4Ca_3Mg_2]^{14+}$.

The MgO_6 octahedron and CaO_8 polyhedra link by sharing edges. The arsenate tetrahedra share their non-OH vertices with MgO_6 octahedra and CaO_8 polyhedra, thereby further bridging these polyhedra. The resulting heteropolyhedral sheet parallel to {001} (Fig. 16) of formula $\{Ca_3Mg_2[AsO_3(OH)]_2[AsO_2(OH)_2]_{10}\}^{4-}$ is pseudohexagonal in general aspect and contains large voids that accommodate the partly occupied OW4a and OW4b H_2O sites. The NaO_6 polyhedron is located in the interlayer region, and two NaO_6 polyhedra share an edge to form a dimer. The shared O vertices of the dimer are H_2O groups (OW1 and OW2; the OW2 being split into two half-occupied sites), and the other five vertices of each Na octahedron (OH4, OH7, OH8 and OH12) are OH groups of the three arsenate groups in the sheets. The $Na_2(OH)_8(H_2O)_2$ dimer thereby links adjacent sheets together in the [001] direction (Fig. 17). An additional isolated H_2O group (OW3) is also located in the interlayer region. The heteropolyhedral sheet and the structure of espadaite as a whole appear to be unique.

Magnesiofluckite

Magnesiofluckite is isostructural with fluckite, $CaMn^{2+}(AsO_3OH)_2(H_2O)_2$. In the structure of magnesiofluckite (Fig. 18), CaO_6 and MgO_6 octahedra each occur as edge-sharing dimers, with equivalent octahedra on either side of a centre of symmetry; Ca_2O_{10} dimers are centred at (0,0,0) and Mg_2O_{10} dimers are centred at (½,0,½). CaO_6 and MgO_6 octahedra also share edges with one another, thereby forming edge-sharing chains parallel to $[10\bar{1}]$ and composed of alternating Ca_2O_{10} and Mg_2O_{10} dimers. These chains are linked in the [101] direction by AsO_3OH groups to form sheets parallel to {010}. The sheets are linked to each other *via* hydrogen bonds.

Picaite

The structure of picaite contains NaO_6 and CaO_6 octahedra and $As1O_3(OH)$ and $As2O_2(OH)_2$ tetrahedra. Both the NaO_6 and CaO_6 octahedra link by sharing edges to form Na_2O_{10} and Ca_2O_{10} dimers, respectively; edge sharing between alternating Na_2O_{10} and Ca_2O_{10} dimers results in a zigzag chain along [101]. The $As1O_3(OH)$ and $As2O_2(OH)_2$ tetrahedra each share one corner with a NaO_6 octahedron and one corner with a CaO_6 octahedron within the same chain of edge-sharing octahedra, resulting in a heteropolyhedral chain (Fig. 19). The remaining two corners of each $As1O_3(OH)$ and $As2O_2(OH)_2$ tetrahedron link to NaO_6 and CaO_6 octahedra in adjacent chains, resulting a framework (Fig. 20). Hydrogen bonds provide additional linkage within this framework. The structure of picaite is unique and we are unaware of any other structure to which it is very similar.

Ríosecoite

The structure of ríosecoite contains one MgO_6 octahedron, one $Ca1O_8$ polyhedron, one $Ca2O_7$ polyhedron and three different $AsO_3(OH)$ tetrahedra (centred by As1, As2 and As3). Two $Ca1O_8$ and two $Ca2O_7$ polyhedra share multiple edges to form

Table 10. Bond-valence analyses for chinchorroite, espadaite, magnesiofluckite, picaite and ríosecoite. Values are expressed in valence units.

Chinchorroite	Na	Mg1	Mg2	Mg3	As1	As2	As3	H bonds	Σ
O1	0.21		0.39		1.37				1.97
O2		0.36$^{\times 2\downarrow}$	0.34		1.32				2.02
O3					1.31			0.24, 0.24, 0.18	1.97
O4					1.02	1.05			2.07
O5				0.33		1.33		0.21, 0.17	2.05
O6		0.34$^{\times 2\downarrow}$	0.29			1.31			1.95
O7			0.30	0.31		1.30			1.90
O8				0.40			1.36	0.18	1.93
O9		0.35$^{\times 2\downarrow}$					1.31	0.17, 0.18	2.01
O10			0.33	0.31			1.26		1.90
OH							1.09	0.14, −0.24	0.99
OW1			0.32					0.17, −0.24, −0.21	0.04
OW2	0.16			0.28				−0.17, −0.18	0.09
OW3	0.18							0.17, −0.17, −0.17	0.01
OW4	0.23, 0.14							−0.18, −0.17	0.03
OW5				0.34				−0.14, −0.18	0.03
Σ	0.93	2.10	1.98	1.97	5.01	4.99	5.01		

Espadaite	Na	Mg	Ca1	Ca2	As1	As2	As3	H bonds	Σ
O1				0.32$^{\times 2\downarrow}$	1.32			0.40	2.04
O2		0.34$^{\times 2\downarrow}$		0.22$^{\times 2\downarrow}$	1.31				1.87
OH3*					1.21			0.19, 0.23, ±0.50	1.13/2.13
OH4	0.15				1.13			−0.34	0.94
O5		0.38$^{\times 2\downarrow}$		0.17$^{\times 2\downarrow}$		1.33			1.88
O6			0.26$^{\times 4\downarrow}$			1.32		0.15, 0.34	2.07
OH7	0.15					1.22		−0.40	0.97
OH8	0.09					1.11		−0.23	0.97
O9				0.31$^{\times 2\downarrow}$			1.41	0.34	2.06
O10		0.33$^{\times 2\downarrow}$	0.19$^{\times 4\downarrow}$				1.33		1.85
OH11							1.19	0.17, −0.34	1.02
OH12	0.16						1.11	−0.14	1.13
OW1	0.20$^{\times 2\rightarrow}$							−0.15$^{\times 2}$	0.10
OW2	0.22$^{\times \frac{1}{2}\downarrow}$, 0.14$^{\times \frac{1}{2}\downarrow}$							−0.13, −0.17	0.04
OW3								0.14$^{\times 2}$, −0.19$^{\times 2}$	0.00
Σ	0.93	2.10	1.80	2.02	4.97	4.97	5.03		

* A symmetrical hydrogen bound between OH3 sites results in ½ OH character for this site.

Magnesiofluckite	Ca	Mg	As1	As2	H bonds	Σ
OH1			1.06		−0.14	0.92
O2	0.37, 0.36		1.34			2.07
O3	0.32	0.32	1.27		0.14	2.05
O4		0.33	1.30		0.28	1.91
O5	0.36			1.35	0.26	1.97
O6	0.29	0.31		1.29		1.89
O7		0.33, 0.27		1.27		1.87
OH8				1.10	0.16, 0.16, −0.28	1.14
OW9	0.33				−0.16, −0.16	0.01
OW10		0.37			−0.16, −0.26, 0.12	0.07
Σ	2.03	1.93	4.97	5.01		

Picaite	Ca	Na	As1	As2	H bonds	Σ
O1	0.34	0.21	1.41			1.96
O2	0.32, 030		1.35			1.97
OH3		0.15	1.16		−0.31	1.00
OH4		0.16, 0.06	1.10		−0.27	1.05
O5	0.37	0.23		1.38		1.98
O6	0.38			1.35	0.31	2.04
O7	0.32			1.25	0.27, 0.22	2.06
OH8		0.21		1.10	−0.22	1.09
Σ	2.03	1.03	5.02	5.08		

Ríosecoite	Mg	Ca1	Ca2	As1	As2	As3	H bonds	Σ
O1		0.26	0.35	1.36				1.97
O2		0.35	0.29	1.34				1.98
O3	0.33		0.18	1.28			0.26	2.05
OH4		0.24		1.07			−0.24	1.07
O5	0.30	0.27			1.32			1.89
O6	0.29		0.25		1.30			1.84
O7	0.35				1.29		0.21, 0.15	2.00
OH8					1.08		0.21, −0.20	1.09
O9			0.28			1.35	0.24	1.87
O10	0.31	0.32				1.32		1.95
O11		0.26	0.27, 0.21			1.27		2.01
OH12		0.09				1.05	0.20, −0.21	1.13
OW13	0.39						−0.21, −0.22	−0.06
OW14		0.25					0.22, −0.15, −0.26	0.06
Σ	1.97	2.04	1.83	5.05	4.99	4.99		

Bond-valence parameters are from Gagné and Hawthorne (2015). Hydrogen-bond strengths are based on O–O bond lengths from Ferraris and Ivaldi (1988). For espadaite, multiplicities are indicated by ×↓→ and hydrogen-bond contributions are not included.

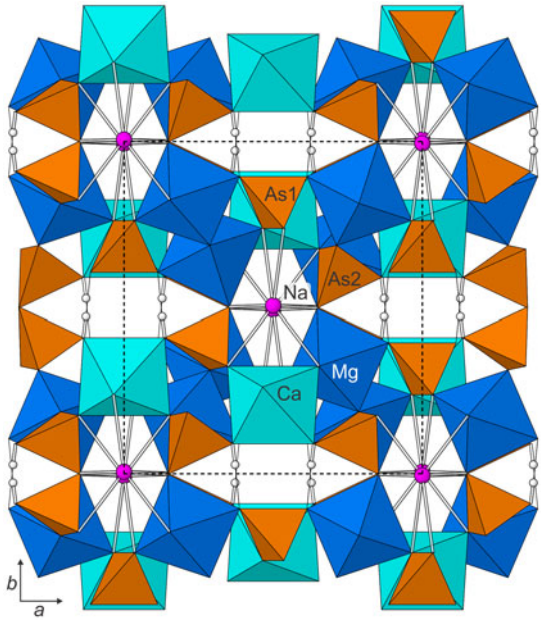

Fig. 12. The crystal structure of camanchacaite (based on that of isostructural canutite) viewed down [001]. Unit cell shown by dashed line. Na–O bonds shown as sticks. Hydrogen bonds shown as solid lines.

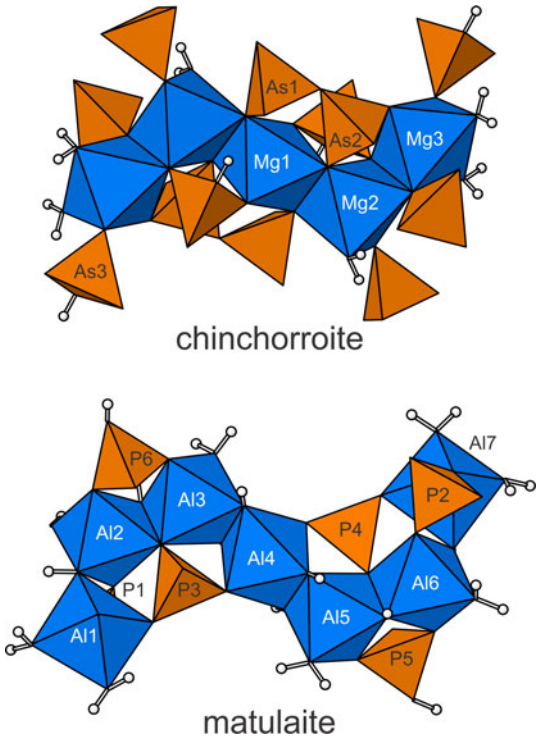

Fig. 13. The abbreviated chains of edge-sharing octahedra with surrounding polyhedra in the structures of chinchorroite and matulaite.

a tetramer (Fig. 21). Each MgO_6 octahedron shares one edge with a $Ca1O_8$ polyhedron and one edge with a $Ca2O_7$ polyhedron, each in a different tetramer, resulting in a chain of edge-sharing polyhedra along [100]. The $As1O_3(OH)$ tetrahedra further link the polyhedra within the chain. The complex chains composed of MgO_6 octahedra, $Ca1O_8$ polyhedra, $Ca2O_7$ polyhedra, and $AsO_3(OH)$ tetrahedra (Fig. 22) are linked to each other by As–O–Mg and As–O–Ca corner links to form a framework (Fig. 23). Hydrogen bonds provide additional linkages within this framework. The structure of ríosecoite is unique and we are unaware of any other structure to which it is very similar.

Discussion

The high levels of arsenic in northern Chile are well documented (*cf.* Tapia *et al.*, 2018). The arsenic, originating most notably from volcanic activity, hot springs and porphyry and epithermal ore

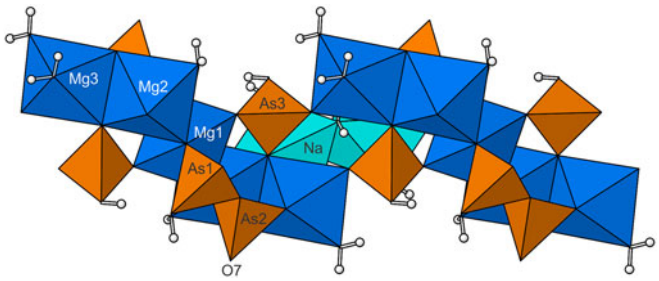

Fig. 14. The thick {10$\bar{1}$} sheet of edge-sharing octahedra with surrounding pyroarsenate and hydrogen-arsenate groups in chinchorroite. Note that O7 vertices link to adjacent sheets. View is down [010].

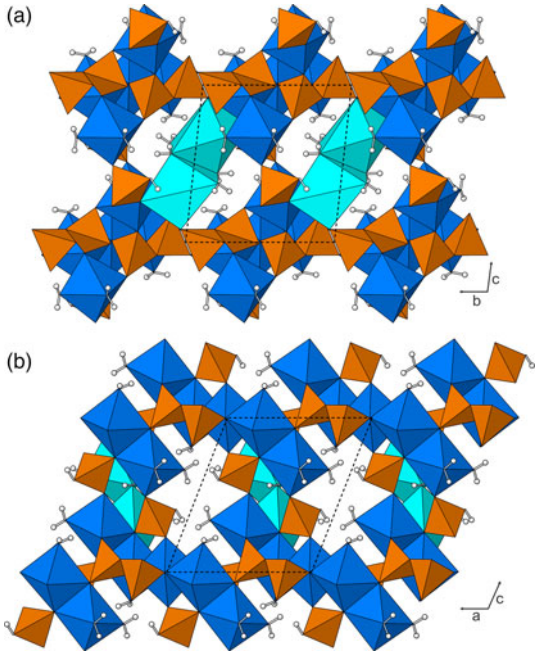

Fig. 15. The structure of chinchorroite (*a*) viewed down [100] and (*b*) viewed down [010].

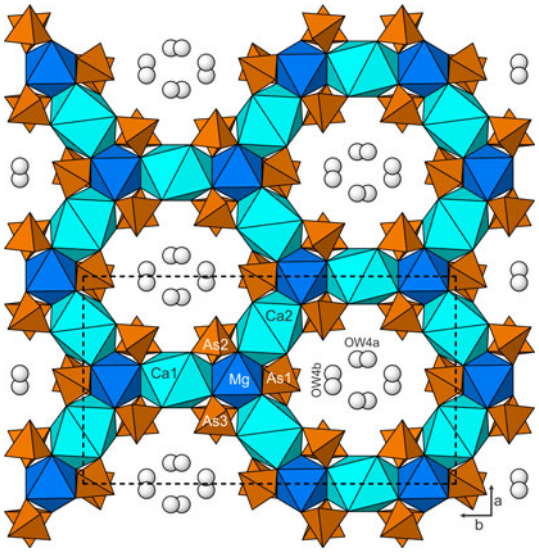

Fig. 16. The heteropolyhedral layer in the structure of espadaite, viewed along [001].

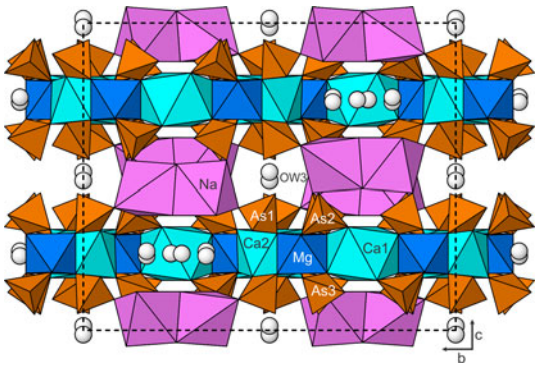

Fig. 17. The structure of espadaite, viewed down [100].

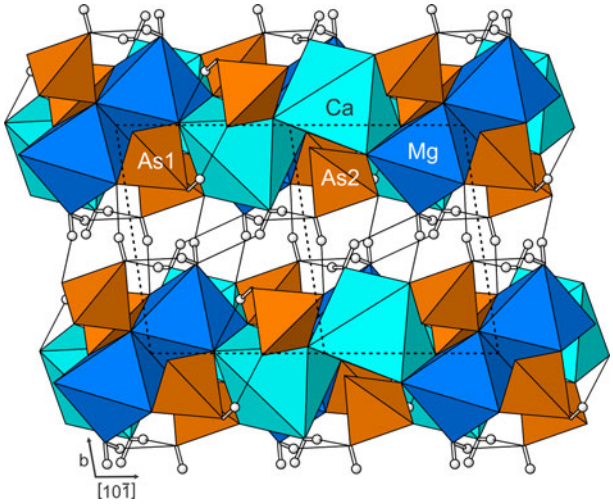

Fig. 18. The structure of magnesiofluckite, viewed down [101].

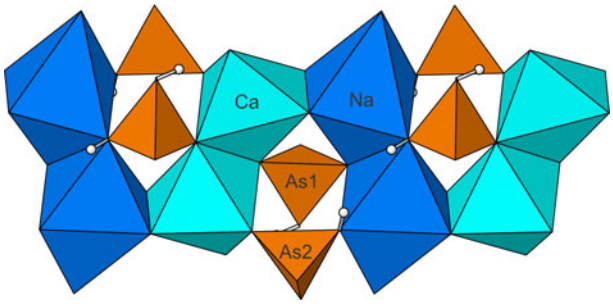

Fig. 19. The chain of edge-sharing octahedra with bridging $As1O_3(OH)$ and $As2O_2(OH)_2$ tetrahedra in the structure of picaite.

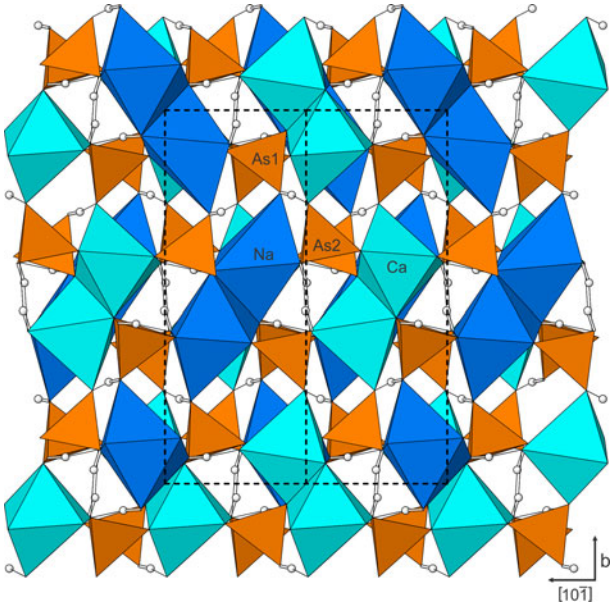

Fig. 20. The structure of picaite viewed down [101], the direction of the chains.

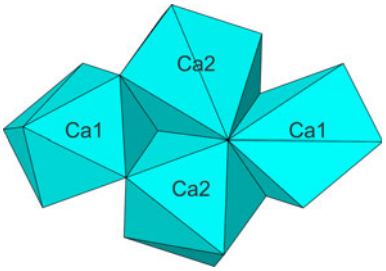

Fig. 21. The tetramer of edge-sharing $Ca1O_8$ and $Ca2O_7$ polyhedra in the structure of ríosecoite.

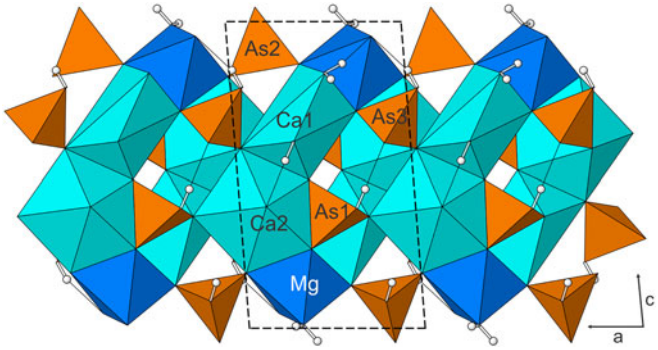

Fig. 22. The complex chain (along **a**) of edge-sharing CaO_7 and CaO_8 polyhedra and MgO_6 octahedra with bridging $AsO_3(OH)$ tetrahedra in the structure of ríosecoite. O–H bonds are shown as sticks and hydrogen bonds as thin lines. The unit cell outline is shown with dashed lines.

deposits over the past 70 million years, once mobilised by weathering, makes its way into drainage systems and groundwater, where it has contributed to deleterious health effects on humans and other organisms dating back at least to the Chinchorro culture (but undoubtedly much earlier) and continuing to this day.

The Torrecillas deposit consists of volcanogenic/hydrothermal veins, variably rich in Cu and/or As, that have been emplaced in metamorphosed marine shales and lavas, perhaps as a skarn-type deposit. Alteration of parts of the veins composed largely of native arsenic has produced an array of arsenites and arsenates (Tables 1 and 2). The hyperarid climate of the Atacama Desert is an important factor in the formation of the secondary mineralisation at Torrecillas, as it is in virtually every ore deposit in the Atacama Desert. The oxidation of native arsenic, and possibly other As-bearing primary phases in the veins, was followed by reaction with fluids rich in dissolved salts. In the Atacama Desert, these saline brines are generally derived from evaporating meteoric water (*cf.* Cameron *et al.*, 2007); however, considering the proximity of the Torrecillas deposit to the Pacific Ocean, it seems possible that the frequent dense coastal camanchaca fogs have also played a role in the alteration of the veins and the formation of the secondary minerals, particularly in the recent past since the exhumation of the deposit well above sea level on Torrecillas Hill. The capacity of salt-rich fog to weather rocks under conditions prevalent in the Atacama Desert has been demonstrated (*cf.* Goudie *et al.*, 2002). Isotopic evidence has shown that significant amounts of Ca and SO_4 in Atacama soils are derived from marine aerosols even in inland areas (100 km or more from the coast) reached by the coastal fogs (Rech *et al.*, 2003). The fogs along the northern Chilean coast are relatively rich in dissolved Na^+, Cl^- and SO_4^{2-}, and also contain significant amounts of Ca^{2+}, Mg^{2+}, K^+, NH_4^+ and NO_3^- (Wang *et al.*, 2014). The frequency of the fogs (up to 189 days per year; Cereceda and Schemenauer, 1991), coupled with the long-term concentration of their salt content under hyperarid conditions, increases the likelihood that they may be a significant factor in the development of the secondary mineralisation at Torrecillas.

Among the As-rich assemblages, some consist of only arsenites, some of both arsenites and arsenates, and some of only arsenates. The localised conditions of Eh, pH and chemical constituents determine the minerals in each assemblage, but none can be considered an equilibrium assemblage. Each assemblage can be considered a snapshot of a dynamically (if slowly) progressing open-system alteration process.

Although arsenites typically predate arsenates, it is not always easy to determine crystallisation sequences. An unusual feature of the Torrecillas secondary arsenic mineral assemblages is the recognition, so far, of twelve new arsenates, all of which contain

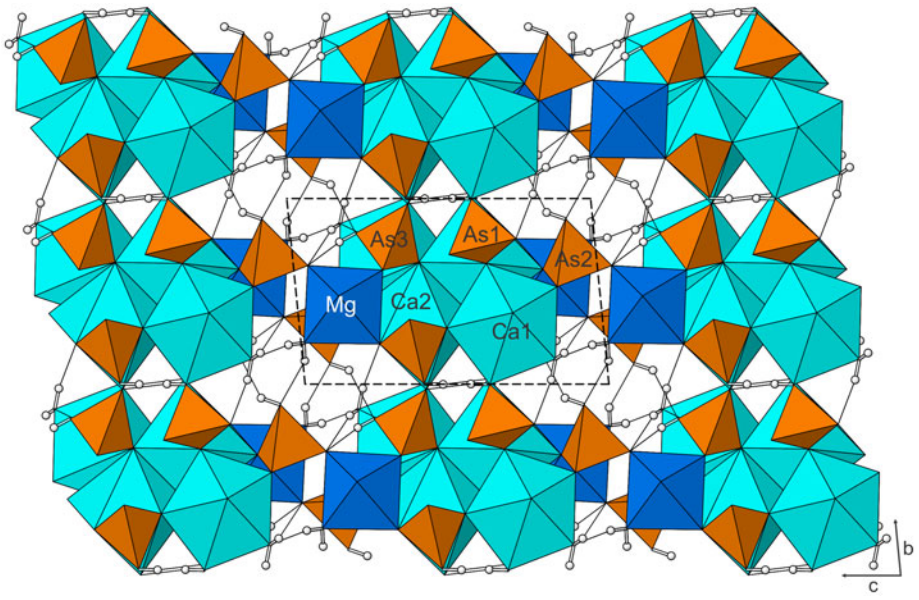

Fig. 23. The structure of ríosecoite viewed down [100], the direction of the chains. O–H bonds are shown as sticks and hydrogen bonds as thin lines. The unit-cell outline is shown with dashed lines.

hydrogen (and/or dihydrogen) arsenate groups; although, among the already known arsenates, there are also normal arsenates. All of the secondary arsenic minerals occurring on the two specimens containing the six new minerals described in this paper are arsenates. Besides the new species camanchacaite, chinchorroite, espadaite, magnesiofluckite, picaite and ríosecoite, other arsenates found on these specimens are talmessite and currierite. The essential cations in these minerals are limited to Ca, Mg and Na. These elements could all be derived from the fog; however, these elements, sourced from altered country rocks, are common constituents of the saline brines noted above. The sequence of crystallisation of the arsenates in the Torrecillas deposit is difficult to determine completely and unambiguously. Talmessite and currierite seem to be earliest, followed by magnesiofluckite and picaite. Camanchacaite seems to occur next in the sequence, but observations suggest that it crystallises over a range and both precedes and postdates the crystallisation of ríosecoite and chinchorroite. The last of these phases to form is espadaite.

It is tempting to try to relate the crystallisation sequence to differences in the compositions and/or structures of the arsenates. Unfortunately, previous studies (*cf.* Magalhães *et al.*, 1988; Majzlan *et al.*, 2014) do not provide much insight that is directly applicable to doing so for the phases at hand. The only straightforward conclusion that can be drawn is that the presence of hydrogen arsenate groups is indicative of crystallisation from solutions of relatively low pH. In this respect, it is worth observing that the saline brines in the region have close to neutral pH (Guillermo Chong Díaz, pers. comm.) and the coastal fogs usually have pH in the neutral to somewhat acid range (Wang *et al.*, 2014). When these fluids interact with reduced phases, such as native As, oxidation tends to produce acids, such as arsenous acid, $H_3As^{3+}O_3$ (less oxidised), and arsenic acid, $H_3As^{5+}O_4$ (more oxidised). The formation of the hydrogen arsenates described herein can be attributed to the evaporation of solutions containing $H_3As^{5+}O_4$, which are also rich in Na^+, Ca^{2+} and Mg^{2+}.

Supplementary material. To view supplementary material for this article, please visit https://doi.org/10.1180/mgm.2019.28

Acknowledgements. Reviewers Frank Hawthorne and Elena Zhitova are thanked for their constructive comments on the manuscript. Guillermo Chong Díaz provided valuable insights, especially regarding the geology and mineral formation. A portion of this study was funded by the John Jago Trelawney Endowment to the Mineral Sciences Department of the Natural History Museum of Los Angeles County.

References

Arriaza B., Amarasiriwardena D., Cornejo L., Standen V., Byrne S., Bartkus L. and Bandak B. (2010) Exploring chronic arsenic poisoning in pre-Columbian Chilean mummies. *Journal of Archeological Science*, **37**, 1274–1278.

Bari H., Cesbron F., Permingeat F. and Pillard F. (1980) La fluckite, arséniate hydraté de calcium et manganèse $CaMnH_2(AsO_4)_2{\cdot}2H_2O$, une nouvelle espèce minérale. *Bulletin de Minéralogie*, **103**, 122–128.

Buchelt M. and Tellez C. (1988) The Jurassic La Negra Formation in the area of Antofagasta, north Chile (lithology, petrography, geochemistry). Pp. 171–182 in: *The southern Central Andes* (H. Bahlburg, C. Breitkreuz and P. Giese, editors). Lecture Notes in Earth Sciences 17. Springer, Berlin–Heidelberg–New York.

Burla M.C., Caliandro R., Camalli M., Carrozzini B., Cascarano G.L., Giacovazzo C., Mallamo M., Mazzone A., Polidori G. and Spagna R. (2012) *SIR*2011: a new package for crystal structure determination and refinement. *Journal of Applied Crystallography*, **45**, 357–361.

Byrne S., Amarasiriwardena D., Bandak B., Bartkus L., Kane J., Jones J., Yañez J., Arriaza B. and Cornejo L. (2010) Were Chinchorros exposed to arsenic? Arsenic determination in Chinchorro mummies' hair by laser ablation inductively coupled plasma-mass spectrometry (LA-ICP-MS). *Microchemical Journal*, **94**, 28–35.

Cameron E.M., Leybourne M.I. and Palacios C. (2007) Atacamite in the oxide zone of copper deposits in northern Chile: involvement of deep formation waters? *Mineralium Deposita*, **42**, 205–218.

Caracas R. and Bobocioiu E. (2011) The WURM project – a freely available web-based repository of computed physical data for minerals. *American Mineralogist*, **96**, 437–443.

Catti M., Chiari G. and Ferraris G. (1980) Fluckite, $CaMn(HAsO_4)_2{\cdot}2H_2O$, a structure related by pseudo-polytypism to krautite $MnHAsO_4{\cdot}2H_2O$. *Bulletin de Minéralogie*, **103**, 129–134.

Cereceda P. and Schemenauer R.S. (1991) The occurrence of fog in Chile. *Journal of Applied Meteorology*, **30**, 1097–1105.

Cooper M.A., Hawthorne F.C., Ball N.A., Ramik R.A. and Roberts A.C. (2009) Groatite, $NaCaMn_2^{2+}(PO_4)[PO_3(OH)]_2$, a new mineral species of the alluaudite group from the Tanco pegmatite, Bernic Lake, Manitoba, Canada: description and crystal structure. *The Canadian Mineralogist*, **47**, 1225–1235.

Ferraris G. and Ivaldi G. (1988) Bond valence vs. bond length in O···O hydrogen bonds. *Acta Crystallographica*, **B44**, 341–344.

Gagné O.C. and Hawthorne F.C. (2015) Comprehensive derivation of bond-valence parameters for ion pairs involving oxygen. *Acta Crystallographica*, **B71**, 562–578.

García F. (1967) Geologia del Norte Grande de Chile. *Simposio Geosinclinal Andino, Sociedad Geológica de Chile Publicaciones*, **3**, 138 pp.

Goudie A.S., Wright E. and Viles H.A. (2002) The roles of salt (sodium nitrate) and fog in weathering: a laboratory simulation of conditions in the northern Atacama Desert, Chile. *Catena*, **48**, 255–266.

Gutiérrez H. (1975) *Informe Sobre una Rápida Visita a la Mina de Arsénico Nativo, Torrecillas*. Instituto de Investigaciones Geológicas, Iquique, Chile.

Higashi T. (2001) *ABSCOR*. Rigaku Corporation, Tokyo.

Kampf A.R., Mills S.J., Rumsey M.S., Spratt J. and Favreau G. (2012) The crystal structure determination and redefinition of matulaite, $Fe^{3+}Al_7(PO_4)_4(PO_3OH)_2(OH)_8(H_2O)_8{\cdot}8H_2O$. *Mineralogical Magazine*, **76**, 517–534.

Kampf A.R., Nash B.P., Dini M. and Molina Donoso A.A. (2013) Magnesiokoritnigite, $Mg(AsO_3OH){\cdot}H_2O$, from the Torrecillas mine, Iquique Province, Chile: the Mg-analogue of koritnigite. *Mineralogical Magazine*, **77**, 3081–3092.

Kampf A.R., Nash B.P., Dini M. and Molina Donoso A.A. (2014*a*) Torrecillasite, $Na(As,Sb)_4^{3+}O_6Cl$, a new mineral from the Torrecillas mine, Iquique Province, Chile: description and crystal structure. *Mineralogical Magazine*, **78**, 747–755.

Kampf A.R., Mills S.J., Hatert F., Nash B.P., Dini M. and Molina Donoso A.A. (2014*b*) Canutite, $NaMn_3[AsO_4]_2[AsO_2(OH)_2]$, a new protonated alluaudite-group mineral from the Torrecillas mine, Iquique Province, Chile. *Mineralogical Magazine*, **78**, 787–795.

Kampf A.R., Nash B.P., Dini M. and Molina Donoso A.A. (2016*a*) Gajardoite, $KCa_{0.5}As_4^{3+}O_6Cl_2{\cdot}5H_2O$, a new mineral related to lucabindiite and torrecillasite from the Torrecillas mine, Iquique Province, Chile. *Mineralogical Magazine*, **80**, 1265–1272.

Kampf A.R., Nash B.P., Dini M. and Molina Donoso A.A. (2016*b*) Chongite, $Ca_3Mg_2(AsO_4)_2(AsO_3OH)_2{\cdot}4H_2O$, a new arsenate member of the hureaulite group from the Torrecillas mine, Iquique Province, Chile. *Mineralogical Magazine*, **80**, 1255–1263.

Kampf A.R., Nash B.P., Dini M. and Molina Donoso A.A. (2017*a*) Juansilvaite, $Na_5Al_3[AsO_3(OH)]_4[AsO_2(OH)_2]_2(SO_4)_2{\cdot}4H_2O$, a new arsenate-sulfate from the Torrecillas mine, Iquique Province, Chile. *Mineralogical Magazine*, **81**, 619–628.

Kampf A.R., Mills S.J., Nash B.P., Dini M. and Molina Donoso A.A. (2017*b*) Currierite, $Na_4Ca_3MgAl_4(AsO_3OH)_{12}{\cdot}9H_2O$, a new acid arsenate with ferrinatrite-like heteropolyhedral chains from the Torrecillas mine, Iquique Province, Chile. *Mineralogical Magazine*, **81**, 1141–1149.

Kampf A.R., Nash B.P., Dini M. and Molina Donoso A.A. (2017*c*) Magnesiocanutite, $NaMnMg_2[AsO_4]_2[AsO_2(OH)_2]$, a new protonated

alluaudite-group mineral from the Torrecillas mine, Iquique Province, Chile. *Mineralogical Magazine*, **81**, 1523–1531.

Kampf A.R., Chukanov N.V., Möhn G., Dini M., Molina Donoso A.A. and Friis H. (2018*a*) Cuatrocapaite-(NH_4), IMA 2018-083. CNMNC Newsletter No. 46, December 2018, page 1371; *Mineralogical Magazine*, **82**, 1369–1379.

Kampf A.R., Chukanov N.V., Möhn G., Dini M., Molina Donoso A.A. and Friis H. (2018*b*) Cuatrocapaite-(K), IMA 2018-084. CNMNC Newsletter No. 46, December 2018, page 1372; *Mineralogical Magazine*, **82**, 1369–1379.

Kampf A.R., Nash B.P. and Molina Donoso A.A. (2019) Mauriziodiniite, IMA 2019-036. CNMNC Newsletter No. 51; *Mineralogical Magazine*, **83**, doi: 10.1180/mgm.2019.58.

Keller P. and Hess H. (1988) Die kristallstrukturen von O'Danielit, Na(Zn, $Mg)_3H_2(AsO_4)_3$, und Johillerit, $Na(Mg,Zn)_3Cu(AsO_4)_3$. *Neues Jahrbuch für Mineralogie, Monatshefte*, **1988**, 395–404.

Magalhães M.C.F., de Jesus J.D.P. and Williams P.A. (1988) The chemistry of formation of some secondary arsenate minerals of Cu(II), Zn(II) and Pb(II). *Mineralogical Magazine*, **52**, 679–690.

Majzlan J., Drahota P. and Filippi M. (2014) Parageneses and crystal chemistry of arsenic minerals. Pp. 17–184 in: *Arsenic: Environmental Geochemistry, Mineralogy, and Microbiology* (R.J. Bowell, C.N. Alpers, H.E. Jamieson, D.K. Nordstrom and J. Majzlan, editors). Reviews in Mineralogy and Geochemistry, **79**. Mineralogical Society of America and the Geochemical Society, Chantilly, Virginia, USA.

Mihajlović T., Libowitzky E. and Effenberger H. (2004) Synthesis, crystal structure, infrared and Raman spectra of $Sr_5(As_2O_7)_2(AsO_3OH)$. *Journal of Solid State Chemistry*, **177**, 3963–3970.

Pekov I.V., Koshlyakova N.N., Agakhanov A.A., Zubkova N.V., Belakovskiy D.I., Vigasina M.F., Turchkova A.G., Sidorov E.G. and Pushcharovsky D.Y. (2016) Calciojohillerite, IMA 2016-068. CNMNC Newsletter No. 34, December 2016, page 1317; *Mineralogical Magazine*, **80**, 1315–1321.

Pouchou J.-L. and Pichoir F. (1991) Quantitative analysis of homogeneous or stratified microvolumes applying the model "PAP". Pp. 31–75 in: *Electron Probe Quantification* (K.F.J. Heinrich and D.E. Newbury, editors). Plenum Press, New York.

Rech J.A., Quade J. and Hart W.S. (2003) Isotopic evidence for the source of Ca and S in soil gypsum, anhydrite and calcite in the Atacama Desert, Chile. *Geochimica et Cosmochimica Acta*, **67**, 575–586.

Roberts A.C., Burns P.C., Gault R.A., Criddle A.J. and Feinglos M.N. (2004) Petewilliamsite, $(Ni,Co)_{30}(As_2O_7)_{15}$, a new mineral from Johanngeorgenstadt, Saxony, Germany: description and crystal structure. *Mineralogical Magazine*, **68**, 231–240.

Sarp H. and Černy R. (2001) Theoparacelsite, $Cu_3(OH)_2As_2O_7$, a new mineral: its description and crystal structure. *Arkives de Science Genève*, **54**, 7–14.

Sheldrick G.M. (2015*a*) SHELXT – Integrated space-group and crystal-structure determination. *Acta Crystallographica*, **A71**, 3–8.

Sheldrick G.M. (2015*b*) Crystal structure refinement with *SHELX*. *Acta Crystallographica*, **C71**, 3–8.

Tapia J., González R., Townley B., Oliveros V., Álvarez F., Aguilar G., Menzies A. and Calderón M. (2018) Geology and geochemistry of the Atacama Desert. *Antonie Van Leeuwenhoek*, **111**, 1273–1291.

Wang F., Michalski G., Seo J. and Ge W. (2014) Geochemical, isotopic, and mineralogical constraints on atmospheric deposition in the hyper-arid Atacama Desert, Chile. *Geochimica et Cosmochimica Acta*, **135**, 29–48.